Error-cone intercept modeling and altitude–wind-load synergy in large-aperture (8.6 m) parabolic-trough collectors

Zhaohui Han[a,*], Zengli Dai[a], Renwei Pan[a], Yu Xie[a], Chao Zhu[a]

[a] *SEPCOIII Electric Power Construction Co., Ltd., Qingdao, 266100, Shandong, China*

Abstract

The intercept factor of a parabolic-trough collector is routinely treated as a fixed constant, which obscures how it scales with aperture and with the deployment site. We promote the intercept factor to an analytical error-cone model – an explicit function of aperture, optical error budget, and absorber diameter – and couple it to site altitude through a wind-load-induced slope-error term in which reduced air density at altitude lowers the wind dynamic pressure on the mirror. Sweeping aperture to 8.6 m, the model's geometric intercept (≈ 0.99 for the EuroTrough geometry) is consistent with the peer-reviewed EuroTrough/LS-2 optical record and, after calibrating a single slope-error parameter, matches third-party element-level measurements of two 8.6 m molten-salt collectors (CGN, 80 mm, 0.966; Longteng, 90 mm, ≥ 0.98) to within 1%. The main result is a scaling law we call the altitude–wind synergy: the optical benefit of high-altitude siting grows monotonically with aperture, because a wide aperture both narrows the optical acceptance margin and amplifies wind-load deformation – exactly the term that altitude relieves – so large apertures gain disproportionately. The sign and aperture-scaling of the gain are robust across the full published range of the wind-deformation parameters; its magnitude (illustratively, the intercept gain from sea level to 2801 m rises from about $+2 \times 10^{-3}$ at 5.77 m to $+24 \times 10^{-3}$ at 8.6 m for a representative coefficient) is set by structural parameters not yet measured. Error-cone optics coupled with altitude–wind-load physics is therefore a necessary, analytically reproducible design tool for the large-aperture troughs now being deployed on high plateaus.

Keywords: parabolic trough collector, intercept factor, error cone model, large aperture, wind load, altitude effect

1. Introduction

Parabolic-trough systems are the most commercially mature concentrating solar power technology, and the adoption of molten salt as the heat-transfer fluid has raised operating temperatures and enabled low-cost sensible heat storage [1, 2, 3, 4, 5, 6]. The drive to reduce cost has pushed collector aperture steadily upward – from the 5.77 m LS-3/EuroTrough class to the 7.5 m Ultimate Trough [7] and now to 8.6 m molten-salt collectors entering pilot and demonstration in

---

[*] Corresponding author. Email address: hanzhaohui@sepco3.com.

Email addresses: `hanzhaohui@sepco3.com` (Zhaohui Han), `dzl@sepco3.com` (Zengli Dai), `renwei.pan@sepco3.com` (Renwei Pan), `zhuchao@sepco3.com` (Chao Zhu)

western China [8, 9, 10]. Molten salt has also been demonstrated internationally as a trough-field heat transfer fluid at the 3.5 MWth Évora platform [11]. A wider aperture raises the geometric concentration ratio and cuts the steel and loop count per unit field, but it concentrates the optical performance onto a smaller relative absorber image, making the intercept factor increasingly sensitive to optical error – precisely the regime in which a fixed-value intercept becomes inadequate.

This aperture growth is concentrated in a setting that compounds the optical challenge. Much of the new trough capacity is being built at high elevation, with China now leading global concentrating-solar deployment [12, 13, 10]: the 8.6 m molten-salt collectors noted above are destined for plants at Golmud (350 MW) and Delingha (300 MW) in Qinghai and at Wumatang (50 MW) in Tibet [8, 9], on plateaus between roughly 2800 and 4000 m; Delingha is also the site of a documented commercial trough solar field dynamic model [14]. At those elevations the air is roughly a quarter to a third less dense than at sea level (about 29% at the 2801 m site used for the quantitative results below), which alters both the convective heat loss from the receiver and the wind loading on the mirror. Lower pressure can also raise clear-sky DNI through reduced atmospheric attenuation [15], but that resource-side benefit is outside the scope of this paper. The receiver heat-loss pathway is the subject of the companion paper; the wind-load pathway – how reduced air density feeds back, through wind-induced slope error, into the intercept factor of a large-aperture collector – is the subject here.

In most system-level trough models the intercept factor is nonetheless treated as a constant calibrated to a single collector [16, 17], which hides the aperture dependence that matters at large scale and severs any link to the operating environment; recent trough-modelling effort has likewise concentrated on receiver-side heat transfer rather than aperture-scale optics [18]. Analytical error-cone formulations have long been available [19, 20] but are seldom used to ask how the intercept scales with aperture, and still less how it couples to site conditions such as altitude. Altitude is, in fact, almost absent from trough modelling: the most recent comprehensive review of parabolic-trough heat loss lists neither elevation nor air pressure among its influencing factors [21], while the high-altitude solar-thermal literature mainly treats flat-plate collectors, district-heating collection networks, and pit storage rather than trough optics [22, 23, 24, 25, 26]. Operational field measurements further show that turbulent wind directly affects parabolic-trough structural loads [27], but that wind-load pathway has not been translated into an altitude-dependent intercept factor. The way this pathway strengthens with aperture has therefore not been quantified.

This paper makes the intercept factor an explicit, analytically computed function of aperture, optical error budget, and absorber diameter, and couples it to altitude through a physically grounded wind-load–slope-error term. We (i) build an error-cone intercept model, validate its geometric intercept against the peer-reviewed EuroTrough/LS-2 optical record, and calibrate its slope-error level against third-party measurements of two 8.6 m molten-salt collectors; (ii) introduce an altitude-dependent wind-load coupling bounded by a sensitivity analysis; and (iii) show that the optical benefit of high-altitude siting grows disproportionately with aperture – an altitude–wind synergy that makes 8.6 m collectors especially well suited to high plateaus. The error-cone machinery itself is classical [19, 20]; the contribution is its use to derive an aperture-scaling law for the intercept and to couple that law to air density, turning a static optical calculation into a rule for jointly sizing and siting large-aperture collectors. Heat-transfer-fluid selection, storage, and the broader techno-economics are treated in a companion paper [28]; here the fluid is fixed to molten salt and the focus is the collector's aperture-scale optics.

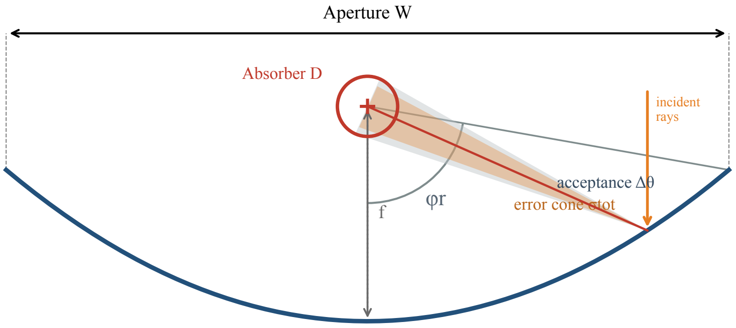

Figure 1: Parabolic-trough optics (not to scale). A collimated ray reflected at a mirror element forms an error cone of RMS width σ_{tot}; the intercept factor γ is the fraction of that cone falling within the local acceptance half-angle $\Delta\theta$ subtended by the absorber. Key geometric quantities: aperture width W, focal length f, rim angle φ_r, and absorber outer diameter D.

2. Error-cone intercept model

The intercept factor γ is the fraction of rays reflected by the mirror that reach the absorber tube. Rather than assign it a fixed value, we compute it analytically with the error-cone formulation of Bendt et al. [19] and Güven and Bannerot [20], which makes γ an explicit function of aperture width W, the optical error budget, and the absorber outer diameter D. This is the property that lets us later couple it to altitude through a single error term (Section 4).

2.1. Collector geometry

The geometry is summarised in Fig. 1. For a parabolic trough of aperture width W and focal length f, the rim angle is

$$\varphi_r = 2\arctan\left(\frac{W}{4f}\right), \tag{1}$$

and the geometric concentration ratio for a cylindrical absorber of outer diameter D is

$$C = \frac{W}{\pi D}. \tag{2}$$

Some industry reports quote the flat-aperture ratio W/D; we use the cylindrical-absorber convention $W/(\pi D)$ throughout. A mirror element at rim angle $\varphi \in [0, \varphi_r]$ lies at a focal distance $s(\varphi) = f\sec^2(\varphi/2)$ from the receiver, so the absorber of radius $R = D/2$ subtends a local acceptance half-angle

$$\Delta\theta(\varphi) = \frac{R}{s(\varphi)} = \frac{R\cos^2(\varphi/2)}{f}. \tag{3}$$

The acceptance half-angle is therefore largest at the vertex and shrinks toward the rim, which is what makes a wider aperture (larger φ_r) progressively harder to intercept. Throughout this paper the focal length is scaled with aperture to hold the rim angle near 80° ($f \approx W/3.36$) – close to the value that maximises collected flux for a cylindrical absorber – so that the aperture comparison is made at fixed rim geometry rather than confounded by a changing rim angle.

2.2. *Optical error budget*

Beam spreading is modelled as a single Gaussian cone of root-mean-square width σ_{tot} that combines the independent contributions of the finite solar width, mirror slope error, specularity, and tracking:

$$\sigma_{\mathrm{tot}}^2 = \sigma_{\mathrm{sun}}^2 + \left(2\sigma_{\mathrm{slope}}\right)^2 + \sigma_{\mathrm{spec}}^2 + \sigma_{\mathrm{track}}^2. \tag{4}$$

The slope error enters with a factor of two because a surface-normal deviation σ_{slope} deflects the reflected ray by $2\sigma_{\mathrm{slope}}$. The four terms are the finite angular width of the solar disc (a 2.8 mrad root-mean-square half-width), the mirror slope error, the specular spread of the reflective surface, and the residual tracking error, with the latter bounded by the solar-position and tracking calculation accuracy [29]. They are added in quadrature because they are mutually independent and each is well approximated by a Gaussian; the convolution of independent Gaussians is itself Gaussian, with variance equal to the sum of variances, which is what collapses the budget to the single effective width σ_{tot} of Eq. (4) and permits the closed form of Eq. (5). Of the four, only the slope error has a structural – and therefore size- and wind-dependent – component; the others are essentially fixed material or celestial properties. The gravity-load slope error $\sigma_{\mathrm{slope,grav}}$ is taken as a fixed structural property (Section 3); in Section 4 we add a wind-load term in quadrature, $\sigma_{\mathrm{slope}}^2 = \sigma_{\mathrm{slope,grav}}^2 + \sigma_{\mathrm{slope,wind}}^2$.

2.3. *Aperture-weighted intercept factor*

For a Gaussian error cone, the fraction of power from a mirror element that falls within the local acceptance half-angle is $\mathrm{erf}(\Delta\theta/(\sqrt{2}\,\sigma_{\mathrm{tot}}))$; this is the convolution of the angular error distribution with the angular size of the absorber, and is exact whenever the individual error sources are independent and approximately Gaussian. Each mirror element must then be weighted by the reflected power it collects. Because the aperture coordinate of an element follows $x = 2f\tan(\varphi/2)$, equal increments of rim angle span an aperture width $\mathrm{d}x = f\sec^2(\varphi/2)\,\mathrm{d}\varphi$; under uniform collimated illumination the collected power per unit rim angle is therefore proportional to $\sec^2(\varphi/2)$. Weighting by this factor and integrating over the rim angle gives the collector intercept factor

$$\gamma = \frac{\displaystyle\int_0^{\varphi_r} \mathrm{erf}\left(\frac{\Delta\theta(\varphi)}{\sqrt{2}\,\sigma_{\mathrm{tot}}}\right)\sec^2(\varphi/2)\,\mathrm{d}\varphi}{\displaystyle\int_0^{\varphi_r}\sec^2(\varphi/2)\,\mathrm{d}\varphi}. \tag{5}$$

A non-random tracking offset μ is handled by replacing the local intercept with $\frac{1}{2}\left[\mathrm{erf}((\Delta\theta + \mu)/(\sqrt{2}\sigma_{\mathrm{tot}})) + \mathrm{erf}((\Delta\theta - \mu)/(\sqrt{2}\sigma_{\mathrm{tot}}))\right]$. Equation (5) is evaluated by trapezoidal quadrature over a uniform 400-point rim-angle grid – at which γ is converged to better than 10^{-5} (doubling the grid changes it by under 10^{-6}, well below the $\sim 10^{-3}$ gains discussed later) – and is implemented as a pure function for independent reproduction (`msptc/optics/intercept.py`; see Data availability). Equation (5) is a purely optical, geometric intercept: it excludes end losses, row-to-row shadowing, soiling, and tracking availability, which are the additional factors folded into the lumped intercepts reported for installed collectors and which we reconcile in Section 3. In the limit $\Delta\theta \gg \sigma_{\mathrm{tot}}$ everywhere – a small aperture or a large absorber – every error function

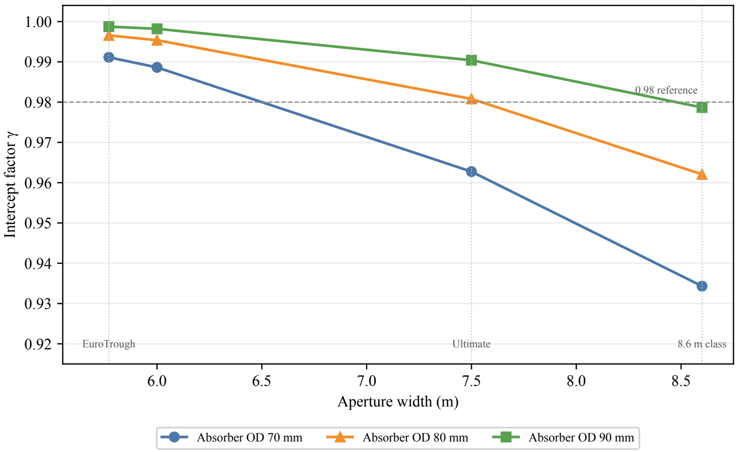

Figure 2: Pure-geometric intercept factor (static optical budget, before the wind loading of Section 4) versus aperture width from the error-cone model, for 70, 80, and 90 mm absorber outer diameters.

saturates and $\gamma \to 1$; the design-relevant regime is the opposite one, in which the rim-angle rays approach $\Delta\theta \sim \sigma_{\text{tot}}$ and the integrand begins to fall below unity.

Figure 2 shows the resulting $\gamma(W)$ for three absorber diameters. At fixed optical error a wider aperture lowers γ, because the rim-angle rays in Eq. (3) see a smaller acceptance angle, while a larger absorber raises γ by enlarging $\Delta\theta$ everywhere. The drop is gradual up to the Ultimate-Trough range and then steepens: with a 70 mm absorber, γ falls from 0.99 at 5.77 m to 0.96 at 7.5 m and 0.93 at 8.6 m, whereas a 90 mm absorber holds it at or above 0.98 across the same span. The 80 mm curve bridges these limits and corresponds to the CGN large-aperture validation point used in Fig. 4. This is the first design lever the model exposes – absorber diameter must scale with aperture to preserve the intercept – and it sits against the opposing trade that a larger aperture raises the concentration ratio (Eq. (2)) and lowers relative thermal loss (Fig. 3), using receiver heat-loss levels consistent with the PTR70 experimental benchmark [30].

3. Validation against measured intercepts

A collector's intercept factor is reported in two distinct senses that must not be conflated. The error-cone model of Section 2 returns a *pure optical-geometric* intercept – the fraction of specularly reflected rays reaching the absorber under the error budget alone. Field and design reports more often quote a *lumped* intercept that additionally folds in end losses, row-to-row shadowing, soiling, and tracking availability, and so sits lower. We validate the model against both, comparing like with like, using the static (wind-free) budget so that the comparison probes the optical quality of the collector rather than its operating wind state.

Because the model computes a pure geometric intercept, the most direct test is against intercepts measured at the solar-collector-element (SCE) level under clean, controlled conditions, where field losses are minimised. Two independent 8.6 m molten-salt collectors have been characterised this way. A single free parameter, the gravity-slope error, is calibrated to them: with $\sigma_{\text{slope,grav}} = 2.5$ mrad the model returns $\gamma = 0.962$ for the CGN 8.6 m / 80 mm collector (measured 0.966) and $\gamma = 0.979$ for the Longteng 8.6 m / 90 mm collector (measured ≥ 0.98) –

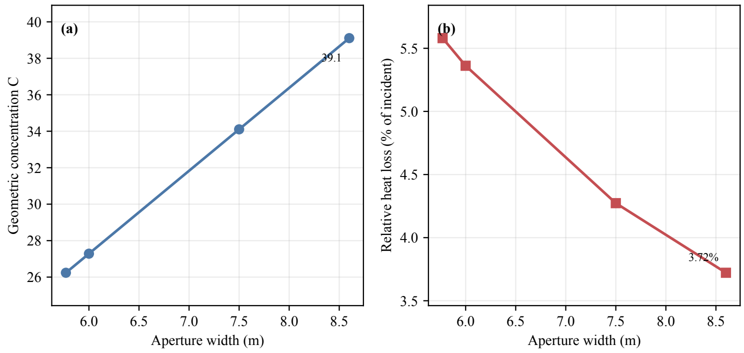

Figure 3: Geometric concentration and relative thermal loss (field heat loss as a fraction of incident power) versus aperture (absorber OD 70 mm). Absolute receiver heat loss is nearly constant, but the collecting area grows with aperture, so a larger aperture both raises the concentration ratio and lowers the relative thermal loss.

within about 1% in each case (Fig. 4). Because one parameter is tuned to two closely spaced targets, this agreement is best read as a calibration and consistency check rather than an independent validation; its value is that a single, physically reasonable slope error – consistent with the EuroTrough/LS-2 record discussed next – simultaneously fits two collectors of *different* absorber diameter. We emphasise that these are *industry-reported* values from a manufacturer pilot and a conference presentation [8, 9], not peer-reviewed measurements, and that they probe the static optical budget rather than the wind coefficients of Section 4. The qualification conditions are nonetheless demanding: the CGN collector was characterised on an outdoor pilot platform with mirror form measured by laser 3D scanning and stable operation reported down to −23 °C and in gale-force wind, while the Longteng intercept was obtained from full-scale loading tests of a complete collector element [9]. This supports reading the reported values as element-level optical intercepts rather than annualised field figures, and so as the right quantity to compare with the model.

The peer-reviewed literature constrains the same geometric intercept indirectly. For the EuroTrough geometry (5.77 m, 70 mm absorber, $f = 1.71$ m – the actual EuroTrough focal length, essentially equal to the scaled $W/3.36$) the model returns $\gamma = 0.991$. This near-unity value is consistent with the high peak optical efficiencies measured for these collectors – 74.1% for EuroTrough ET150 and 73.6% for LS-2 with clean evacuated receivers [31, 32] – once mirror reflectance, glass transmittance, absorptance, cleanliness, shading, and end losses are accounted for separately, as they are in any system model. By contrast, the intercepts of 0.92–0.95 frequently quoted for the same collectors [2] are *lumped* figures that already fold in those field losses; adopting such a value as the geometric intercept while *also* applying cleanliness and shading factors would double-count them. This is why $\sigma_{\text{slope,grav}}$ is anchored to the element-level optical measurements rather than to the lumped field figure: an earlier 3.5 mrad estimate, chosen to force the EuroTrough geometric intercept down into the lumped band, was discarded once the distinction was made explicit. The assumed 2.8 mrad solar RMS half-width – marginally above the ≈ 2.6 mrad Gaussian sunshape commonly adopted for these collectors – and the 2.5 mrad slope error are consistent with the optical and slope-error measurements reported for them [32, 31].

Two caveats bound this validation. First, the only direct numeric intercept comparison is against the 8.6 m industry data; the peer-reviewed literature constrains the geometric intercept

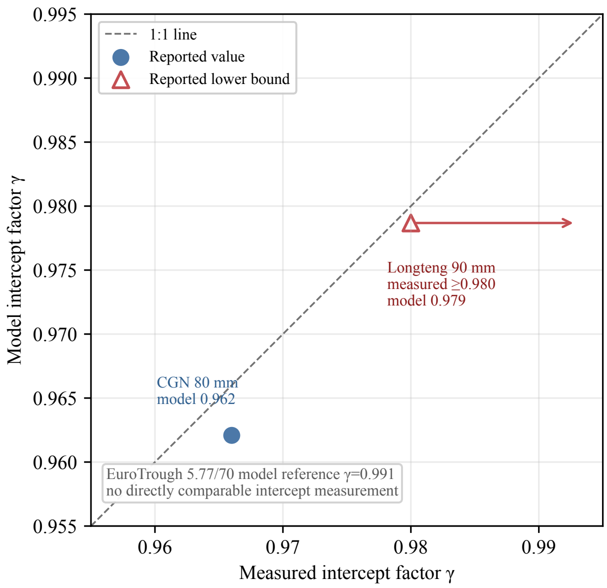

Figure 4: Calibrated model versus measured intercept factor for 8.6 m large-aperture collectors (CGN, 80 mm, $\gamma = 0.966$; Longteng, 90 mm, $\gamma \geq 0.98$, plotted as a lower-bound marker). A single slope-error parameter is fitted to the two points; the model then matches both to within 1%. The EuroTrough geometric intercept (≈ 0.99) is annotated as a model-only reference because no directly comparable element-level intercept measurement is reported.

through optical-efficiency and slope-error measurements but does not itself report a directly comparable element-level intercept. Peer-reviewed intercept measurements of large-aperture collectors would materially strengthen the validation. Second, the measurements validate the static geometric budget only – the wind-load coupling of Section 4 is supported separately by the sensitivity analysis of Section 5.

4. Wind-load–altitude coupling

The intercept model of Section 2 depends on site altitude through exactly one term: the wind-load contribution to mirror slope error. We write the wind-induced slope error as the product of a structural response coefficient, the wind dynamic pressure, and a dimensionless aperture-amplification factor,

$$\sigma_{\text{slope,wind}} = c_w\, q \left(\frac{W}{W_{\text{ref}}}\right)^a, \qquad q = \tfrac{1}{2}\rho(z)\, v_d^2, \tag{6}$$

where q is the dynamic pressure of a design wind speed v_d, W_{ref} a reference aperture, and the exponent a captures how slope deformation grows with aperture for a given structural design. The wind term adds in quadrature to the gravity-load slope error, $\sigma^2_{\text{slope}} = \sigma^2_{\text{slope,grav}} + \sigma^2_{\text{slope,wind}}$, and feeds Eq. (4).

Altitude enters Eq. (6) solely through the air density $\rho(z)$. Treating air as an ideal gas at the ambient design temperature, with the U.S. Standard Atmosphere (1976) [33] pressure–altitude relation setting $p(z)$,

$$\rho(z) = \frac{p(z)}{R_a T}, \qquad p(z) = p_0 \left(1 - 2.25577 \times 10^{-5}\, z\right)^{5.25588}, \tag{7}$$

where $R_a = 287\,\mathrm{J\,kg^{-1}\,K^{-1}}$ and the temperature T is held at its design value, so that altitude enters through the pressure alone. At fixed T the density at Golmud (2801 m) is then about 29% below its sea-level value (the pressure ratio is 0.71), so the wind dynamic pressure q – and with it $\sigma_{\text{slope,wind}}$ – falls by the same factor. A higher site therefore reduces wind-induced slope error and raises γ. This is the optical counterpart of the convective heat-loss reduction reported for the same site in the companion paper; here altitude is admitted *only* through the wind/optical channel, keeping the two studies orthogonal.

The form of Eq. (6) follows from a first-order moment balance rather than a detailed structural model, and the exponent range can be bounded by a simple argument. Wind of dynamic pressure q acting on the aperture exerts a force per unit collector length of order qW, which the space frame transmits to the drive as a torque about the torque-tube axis of order $qW\ell$, where the moment arm ℓ ranges from roughly constant (pressure centre near the tube) to of order W (arm growing with aperture). The torque therefore scales as qW^a with $a \in [1, 2]$. Crucially, the deployed large-aperture collectors hold torsional stiffness roughly *constant* with size – the RT86 8.6 m collector reports a stiffness comparable to the 5.77 m EuroTrough [9] – so the induced slope error, torque divided by a near-constant stiffness, inherits the same W^a growth. (Had stiffness instead been scaled up with size, the wind term would weaken with aperture and there would be no synergy to report; the constant-stiffness regime is what the cited data describe.) This is a falsifiable scope condition rather than a universal structural law: if future full-scale measurements show torsional stiffness increasing strongly with aperture, the altitude–wind synergy predicted here would weaken or disappear for that collector family. Normalising to $W_{\text{ref}} = 5.77$ m places the EuroTrough at unit amplification: at this reference aperture the collector still carries a baseline wind term $c_w q$, and the factor $(W/W_{\text{ref}})^a$ then measures how the wind-load slope error of a *larger* collector grows relative to that baseline. This nonzero baseline is why the sea-level-to-Golmud intercept gain in Fig. 5 is already small but finite ($+1.9 \times 10^{-3}$) at 5.77 m. The exponent bracket $a \in [1, 2]$ is exactly this moment-arm range, and the sensitivity analysis spans it. The air density itself falls smoothly with elevation, to 0.89, 0.78, and 0.71 of its sea-level value at 1000, 2000, and 2801 m, so a plant on the Qinghai–Tibet plateau operates under roughly three-quarters of the sea-level wind loading at any given wind speed.

The solar, specularity, tracking, and gravity-slope terms are fixed optical properties (Table 1). The coefficient c_w, by contrast, sets the absolute deformation per unit dynamic pressure of a particular structure and cannot be inferred from the static intercept measurements of Section 3; we therefore treat it as a representative engineering coefficient and report results across a sensitivity band rather than at a single value. The central curves use $c_w = 1.7 \times 10^{-5}\,\mathrm{rad\,Pa^{-1}}$ and $a = 1.5$; the band $c_w \in [1.0, 2.5] \times 10^{-5}$ and $a \in [1.0, 2.0]$ (Table 1) is what bounds the synergy of Section 5. Because c_w is unmeasured, we draw no conclusion from the absolute magnitude of the predicted gain – only from its sign and its growth with aperture, both of which hold across the entire band. Because the synergy is the *difference* in intercept between two elevations at a common design wind speed, v_d enters the dynamic pressure identically at both sites and sets only the overall magnitude of $\Delta\gamma$; it does not change the sign or aperture-scaling that we interpret.

Table 1: Optical error budget and wind-load coupling parameters. The solar, specularity, and tracking terms and the gravity-load slope error are fixed inputs ($\sigma_{\text{slope,grav}}$ back-calibrated in Section 3); c_w and a are representative engineering coefficients bounded by a sensitivity band rather than measured directly.

Parameter	Symbol	Default	Range	Basis
Solar beam spread	σ_{sun}	2.8 mrad	—	fixed optical input
Gravity slope error	$\sigma_{\text{slope,grav}}$	2.5 mrad	—	back-calibrated (Section 3)
Specularity error	σ_{spec}	1.0 mrad	—	fixed optical input
Tracking error	σ_{track}	1.0 mrad	—	fixed optical input
Reference aperture	W_{ref}	5.77 m	—	EuroTrough geometry
Design wind speed	v_d	$10\,\text{m}\,\text{s}^{-1}$	—	nominal operating wind
Wind-response coeff.	c_w	1.7×10^{-5} $\text{rad}\,\text{Pa}^{-1}$	$1.0\text{–}2.5 \times 10^{-5}$	stiffness-constrained
Aperture exponent	a	1.5	1.0–2.0	engineering scaling

5. Altitude–wind synergy

Combining the aperture dependence of the intercept factor (Section 2) with the density dependence of the wind-load term (Section 4) yields the central result of this paper: the optical benefit of high-altitude siting is not uniform across collector sizes but grows with aperture. Figure 5 plots the intercept-factor gain $\Delta\gamma = \gamma(2801\,\text{m}) - \gamma(0\,\text{m})$ against aperture for a fixed 70 mm absorber, isolating aperture as the sole variable. Both intercepts in each pair carry the operating-wind load of Section 4, so each sea-level value lies below the wind-free intercept of Fig. 2; the synergy is the change between them. The gain rises monotonically and strongly super-linearly with aperture; for the representative coefficients of Table 1 it is $+1.9$, $+12.0$, and $+24.3 \times 10^{-3}$ at 5.77, 7.5, and 8.6 m – more than an order of magnitude larger for the large-aperture collector than for the EuroTrough-class reference. These magnitudes are illustrative: they scale with the unmeasured c_w (Section 4), so the robust content of the figure is the monotone, super-linear *growth* of the gain with aperture, not its absolute size.

The mechanism follows directly from the model. Slope error enters γ through the acceptance margin $\Delta\theta/\sigma_{\text{tot}}$ (Eq. (5)); at a wide aperture the rim-angle rays have the smallest margin (Eq. (3)), so γ there is the most sensitive to any change in σ_{tot}. The wind contribution to σ_{tot} is itself amplified by aperture through $(W/W_{\text{ref}})^a$ (Eq. (6)), and altitude relieves precisely this term. The two aperture dependencies compound: the collector most penalized by wind-load slope error at sea level is also the one that gains the most when reduced air density removes that penalty. Large-aperture troughs are therefore disproportionately favoured by high-altitude siting on the optical channel alone – before the convective heat-loss reduction quantified in the companion paper is added. The 70 mm absorber is used in Fig. 5 only to isolate the aperture scaling; deployed 8.6 m collectors adopt 80–90 mm tubes that lift the absolute intercept back above 0.95 (Fig. 4).

This conclusion is robust to the uncertainty in the wind parameters. Across the full sensitivity band of Table 1 – the nine (c_w, a) combinations – the 8.6 m altitude gain remains strictly positive: for the 70 mm geometry of Fig. 5 it spans $+5.7$ to $+67.2 \times 10^{-3}$ (central value $+24.3$), and for the deployed 90 mm configuration $+2.8$ to $+47.7 \times 10^{-3}$ (central $+13.5$). The sign of the synergy never reverses, even though its magnitude varies by an order of magnitude with c_w and a; the claim is thus a first-order design rule, not an artefact of a single parameter choice. The wide

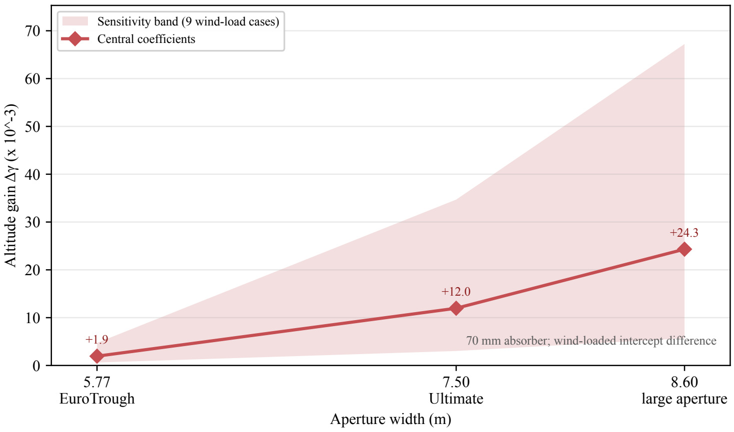

Figure 5: Altitude–wind synergy: the intercept-factor gain $\Delta\gamma$ from sea level to Golmud grows with aperture (+1.9, +12.0, +24.3 $\times 10^{-3}$ at 5.77, 7.5, 8.6 m), evidencing disproportionate benefit for large apertures. Absorber fixed at 70 mm to isolate aperture as the sole variable. The shaded band spans the nine (c_w, a) wind-load cases of Table 1; each $\Delta\gamma$ value is the difference between the Golmud and sea-level wind-loaded intercepts at the same design wind speed ($v_d = 10\,\mathrm{m\,s^{-1}}$).

magnitude range is also why we present the effect as a scaling law and a sign, and defer an absolute prediction to a structural characterisation of the specific collector.

6. Discussion

6.1. *Analytical error cone versus ray tracing*

The error-cone integral of Eq. (5) is the analytical counterpart of the Monte-Carlo ray tracing routinely used to evaluate trough optics. Both take the same physical inputs – a solar angular profile and a slope/specularity/tracking error budget – but the analytical form returns the intercept in closed quadrature, at negligible cost and free of statistical noise, which is what makes the aperture and altitude sweeps of this paper, and their sensitivity bands, tractable. Its price is the Gaussian, axisymmetric error assumption of Eq. (4): it cannot represent a structured slope-error map, astigmatism that varies along the collector, or non-Gaussian specular tails. For the design-stage questions addressed here – how the intercept scales with aperture and how it responds to a change in air density – these are second order; a structured ray trace would refine the absolute intercept but would inherit the same aperture and density dependences that drive the synergy.

6.2. *Design implications*

Three levers follow from the model. First, absorber diameter must scale with aperture: Fig. 2 shows that holding a 70 mm tube while widening the aperture to 8.6 m costs about six points of geometric intercept, almost all of which an 80–90 mm tube recovers – consistent with the absorber choices of the deployed collectors. Second, the concentration ratio rises with aperture (Eq. (2)), so a larger tube erodes the thermal advantage more slowly than it erodes the optical one, and the two can be balanced rather than traded one-for-one. Third, and least intuitively, siting interacts with size: because the altitude gain in intercept grows with aperture (Section 5), the largest collectors are precisely those whose optical performance benefits most from a high-altitude site. A developer choosing a collector size for a plateau plant therefore has an optical reason – independent of the thermal and economic arguments of the companion paper – to prefer the larger aperture.

6.3. Why a constant intercept misleads at scale

Fixing the intercept to a single calibrated value, as standard trough system models do [16, 17], is adequate when aperture and site stay near the collector for which it was calibrated. It fails in exactly the regime this paper targets: extrapolated to 8.6 m a constant misses the steep, absorber-dependent decline of Fig. 2, and being site-blind it discards the altitude synergy altogether. Promoting the intercept to an analytical function of aperture, error budget, and air density restores both dependences for the cost of a single quadrature, and does so transparently enough to be reproduced and audited from the published code.

6.4. Limitations and outlook

Three limitations point to the natural next steps. The wind coupling is a scaling law calibrated to published stiffness data, not a structural model; a finite-element or wind-tunnel characterisation of a specific 8.6 m collector would replace the sensitivity band of Table 1 with a single calibrated curve and convert the synergy from a sign-and-scaling statement into an absolute prediction. The Gaussian error budget could likewise be relaxed: a measured slope-error map propagated through a ray trace would test whether real large-aperture mirrors depart from the axisymmetric assumption in a way that matters for the intercept. Finally, the optical synergy quantified here adds to, but is reported separately from, the convective-loss and freeze-protection effects of the companion paper; a unified high-altitude collector model carrying both channels would let the two be optimised together and would extend naturally to the 13 m apertures already on manufacturers' roadmaps.

7. Conclusions

We have promoted the parabolic-trough intercept factor from a fixed constant to an analytical error-cone function of aperture, optical error budget, and absorber diameter, and coupled it to site altitude through a single wind-load–slope-error term. After calibrating a single slope-error parameter, the model matches third-party measurements of two 8.6 m molten-salt collectors to within about 1%, with a geometric intercept consistent with the peer-reviewed EuroTrough/LS-2 optical record.

The central finding is a scaling law – the altitude–wind synergy. Because a wide aperture both narrows the acceptance margin and amplifies wind-load slope error, the intercept gain from reduced air density grows monotonically and super-linearly with aperture. Its sign and aperture-scaling are robust across the full sensitivity band of the wind parameters, making them a first-order design rule; the absolute magnitude (illustratively $\sim +24\times10^{-3}$ at 8.6 m for a representative coefficient) awaits a structural measurement of c_w. Either way, large-aperture troughs are optically well matched to high-altitude sites.

These results rest on a wind coupling calibrated to published stiffness data rather than measured directly, and on a validation that leans partly on industry-reported intercepts; both are bounded – by the sensitivity analysis and by the peer-reviewed optical record respectively – and the routes to tightening them are set out in Section 6. Within these bounds, the coupled error-cone/altitude framework offers an analytically reproducible, first-order optical design tool for the large-aperture high-altitude troughs now entering deployment.

Nomenclature

Latin symbols	
a	aperture-amplification exponent (–)
C	geometric concentration ratio (–)
c_w	wind-load response coefficient (rad Pa^{-1})
D	absorber outer diameter (m)
f	focal length (m)
p	air pressure (Pa)
q	wind dynamic pressure (Pa)
R	absorber outer radius, $D/2$ (m)
R_a	specific gas constant of air (J kg^{-1} K^{-1})
s	focal distance of a mirror element (m)
T	absolute temperature (K)
v_d	design wind speed (m s^{-1})
W	aperture width (m)
x	aperture-plane coordinate (m)
z	site elevation (m)
Greek symbols	
γ	intercept factor (–)
$\Delta\gamma$	altitude gain in intercept factor (–)
$\Delta\theta$	local acceptance half-angle (rad)
μ	non-random tracking offset (rad)
ρ	air density (kg m^{-3})
σ_{tot}	total RMS optical beam error (rad)
σ_{sun}	solar RMS angular half-width (rad)
σ_{slope}	mirror slope error (rad)
σ_{spec}	specularity error (rad)
σ_{track}	tracking error (rad)
φ	rim-angle coordinate (rad)
φ_r	rim angle (rad)
Subscripts	
grav	gravity-load component
ref	reference collector (EuroTrough, 5.77 m)
tot	total
wind	wind-load component
0	sea level
Abbreviations	
CSP	concentrating solar power
OD	(absorber) outer diameter
RMS	root mean square
SCE	solar collector element

Declaration of generative AI and AI-assisted technologies in the manuscript preparation process

During the preparation of this work the authors used ChatGPT (OpenAI) and Claude (Anthropic) to assist with programming and computation, language editing of the manuscript, and organising and producing figures. No AI tool was used to generate the underlying simulation data or model, or to draw the scientific conclusions, which are the authors' own. After using these tools, the authors reviewed and edited the content as needed and take full responsibility for the content of the published article.

CRediT authorship contribution statement

Zhaohui Han: Conceptualization, Methodology, Formal analysis, Visualization, Writing – original draft. **Zengli Dai:** Supervision, Resources, Funding acquisition, Writing – review & editing. **Renwei Pan:** Methodology, Supervision, Project administration. **Yu Xie:** Investigation, Writing – review & editing, Software. **Chao Zhu:** Validation, Data curation, Writing – review & editing. All authors have read and agreed to the published version of the manuscript.

Declaration of competing interest

The authors are employed by SEPCOIII Electric Power Construction Co., Ltd. This research was funded by POWERCHINA GROUP (grant number DJ-ZDXM-2025-19), the parent company of SEPCOIII Electric Power Construction Co., Ltd. The authors declare no other financial interests or personal relationships that could have appeared to influence the work reported in this paper.

Funding

This research was funded by POWERCHINA GROUP, grant number DJ-ZDXM-2025-19.

Data availability

The simulation code (`msptc`) is openly available at `https://github.com/han348661657/msptc` (MIT License) and archived at Zenodo (DOI: `https://doi.org/10.5281/zenodo.20896806`). The archived package contains the model source code, default configuration, and the analysis and plotting scripts that regenerate the figures and derived tables reported here.

References

[1] S. A. Kalogirou, Solar thermal collectors and applications, Progress in Energy and Combustion Science 30 (3) (2004) 231–295. `doi:10.1016/j.pecs.2004.02.001`.

[2] H. Price, E. Lüpfert, D. Kearney, E. Zarza, G. Cohen, R. Gee, R. Mahoney, Advances in parabolic trough solar power technology, Journal of Solar Energy Engineering 124 (2) (2002) 109–125. `doi:10.1115/1.1467922`.

[3] A. Fernández-García, E. Zarza, L. Valenzuela, M. Pérez, Parabolic-trough solar collectors and their applications, Renewable and Sustainable Energy Reviews 14 (7) (2010) 1695–1721. `doi:10.1016/j.rser.2010.03.012`.

[4] D. Kearney, U. Herrmann, P. Nava, B. Kelly, R. Mahoney, J. Pacheco, R. Cable, N. Potrovitza, D. Blake, H. Price, Assessment of a molten salt heat transfer fluid in a parabolic trough solar field, Journal of Solar Energy Engineering 125 (2) (2003) 170–176. `doi:10.1115/1.1565087`.

[5] U. Herrmann, D. W. Kearney, Survey of thermal energy storage for parabolic trough power plants, Journal of Solar Energy Engineering 124 (2) (2002) 145–152. `doi:10.1115/1.1467601`.

[6] K. Vignarooban, X. Xu, A. Arvay, K. Hsu, A. M. Kannan, Heat transfer fluids for concentrating solar power systems – a review, Applied Energy 146 (2015) 383–396. `doi:10.1016/j.apenergy.2015.01.125`.

[7] W. Schiel, M. Geyer, Ultimate trough – the new parabolic trough collector generation for large commercial solar power plants, SBP/Flabeg technical material (2007).

[8] China General Nuclear Power Group, Technical verification of an 8.6 m molten-salt parabolic-trough collector system in qinghai, Corporate news release, industry-reported, non-peer-reviewed source; 8.6 m CGN collector with third-party SCE intercept factor 0.966. `https://www.cgnpc.com.cn/cgn/c100944/2026-04/24/content_f27a0be6712b40c28ee37fa85d588f6b.shtml` (2026).

[9] Longteng Solar Thermal, RT86 molten-salt large-aperture trough demonstration system: key equipment technology and application prospects, CSPPLAZA molten-salt energy-storage commercialization forum presentation, industry-reported, non-peer-reviewed source; reports RT86 8.6 m collector compatibility with 80–90 mm receivers, intercept factor $\geq$ 0.98 for 90 mm receivers, and torsional stiffness comparable to conventional EuroTrough-class collectors. `http://www.royalcsp.com/h-nd-271.html` (2025).

[10] National Solar Thermal Power Industry Technology Innovation Strategic Alliance, Solar Thermal Power Professional Committee, China Renewable Energy Society, F. Du, Z. Wang, Y. He, Blue book of China's concentrating solar power industry, Advanced Technology of Electrical Engineering and Energy 45 (2) (2025) 1–45. `doi:10.12067/ATEEE2601019`.

[11] N. Dicke, M. Meyer-Grünefeldt, M. Wittmann, J. Stengler, P. Horta, P. Martins, M. Torabzadegan, K. Schmitz, M. Schmitz, N. Gathmann, C. Stefan, Demonstration of 3.5 MWth parabolic trough with ternary molten salt at the évora molten salt platform, in: SolarPACES Conference Proceedings, Vol. 1, 2024. `doi:10.52825/solarpaces.v1i.640`.

[12] IEA SolarPACES, IEA SolarPACES annual report 2022, Tech. rep., International Energy Agency SolarPACES, `https://www.solarpaces.org/csp-research/` (2023).

[13] B. Lynch, H. Metghalchi, Y. Levendis, Concentrating solar thermal power in china: 2025 review and outlook, ASME Open Journal of Engineering 4 (2025) 040807. `doi:10.1115/1.4070013`.

[14] S. Lengge, X. Ershu, T. Jianfang, D. Jun, Z. Dongming, X. Hui, Z. Yanan, Y. Gang, H. Hongjuan, Study on dynamic model and dynamic characteristics of Delingha 50 MW trough solar field, Applied Thermal Engineering 215 (2022) 118943. `doi:10.1016/j.applthermaleng.2022.118943`.

[15] C. A. Gueymard, REST2: High-performance solar radiation model for cloudless-sky irradiance, illuminance, and photosynthetically active radiation – validation with a benchmark dataset, Solar Energy 82 (3) (2008) 272–285. `doi:10.1016/j.solener.2007.04.008`.

[16] R. Forristall, Heat transfer analysis and modeling for a parabolic trough solar receiver implemented in engineering equation solver, National Renewable Energy Laboratory Technical Report NREL/TP-550-34169 (2003). `doi:10.2172/15004820`.

[17] M. J. Wagner, P. Gilman, Technical manual for the SAM physical trough model, National Renewable Energy Laboratory Technical Report NREL/TP-5500-51825 (2011). `doi:10.2172/1016437`.

[18] G. Ou, P. Liu, Z. Liu, W. Liu, Performance analyses and heat transfer optimization of parabolic trough receiver with a novel single conical strip insert, Renewable Energy 199 (2022) 335–350. `doi:10.1016/j.renene.2022.08.131`.

[19] P. Bendt, A. Rabl, H. W. Gaul, K. A. Reed, Optical analysis and optimization of line focus solar collectors, Tech. Rep. SERI/TR-34-092, Solar Energy Research Institute (1979).

[20] H. M. Güven, R. B. Bannerot, Determination of error tolerances for the optical design of parabolic troughs for developing countries, Solar Energy 36 (6) (1986) 535–550.

[21] P. Alamdari, M. Khatamifar, W. Lin, Heat loss analysis review: Parabolic trough and linear fresnel collectors, Renewable and Sustainable Energy Reviews 199 (2024) 114497. `doi:10.1016/j.rser.2024.114497`.

[22] D. Wang, Z. Mo, Y. Liu, Y. Ren, J. Fan, Thermal performance analysis of large-scale flat plate solar collectors and regional applicability in China, Energy 238 (2022) 121931. `doi:10.1016/j.energy.2021.121931`.

[23] D. Wang, B. Fan, Y. Chen, Y. Han, Y. Liu, Y. Wang, H. Liu, X. Jiao, Comparative analysis of heat loss performance of flat plate solar collectors at different altitudes, Solar Energy 244 (2022) 490–506. `doi:10.1016/j.solener.2022.08.060`.

[24] H. Chen, B. Wang, C. Song, D. Wang, Y. Liu, Heat losses in directly buried solar heat collection networks in high-altitude regions, Solar Energy 290 (2025) 113384. `doi:10.1016/j.solener.2025.113384`.

[25] H. Liu, D. Wang, Y. Liu, Y. Li, M. Gao, J. Fan, M. Wei, L. Liu, Thermal storage and loss characteristics of underground water pits of solar district heating systems in Xizang plateau, Energy 308 (2024) 132702. `doi:10.1016/j.energy.2024.132702`.

[26] Q. Zeng, L. Li, X. Chen, Z. Tian, H. Mao, Y. Luo, C. Zhou, J. Fan, Techno-economic performance and optimization of a large solar district heating system with pit storage under Tibetan plateau, Energy 315 (2025) 134449. `doi:10.1016/j.energy.2025.134449`.

[27] U. Egerer, S. Dana, D. Jager, B. J. Stanislawski, G. Xia, S. Yellapantula, Field measurements reveal insights into the impact of turbulent wind on loads experienced by parabolic trough solar collectors, preprint; operational field measurements of wind and structural loads in a parabolic-trough CSP field. (2024). `arXiv:2401.13089`.

[28] Z. Han, Z. Dai, Y. Wei, R. Pan, Y. Xie, D. Wang, Freeze-protection economics can reverse the heat-transfer-fluid preference for cold high-altitude parabolic-trough concentrating solar power: a four-dimensional (4e) and thermal-storage market-value assessment, Companion paper, under review, companion manuscript (2026).

[29] I. Reda, A. Andreas, Solar position algorithm for solar radiation applications, Solar Energy 76 (5) (2004) 577–589. `doi:10.1016/j.solener.2003.12.003`.

[30] F. Burkholder, C. Kutscher, Heat loss testing of Schott's 2008 PTR70 parabolic trough receiver, Tech. Rep. NREL/TP-550-45633, National Renewable Energy Laboratory (2009). `doi:10.2172/1369635`.

[31] E. Lüpfert, M. Geyer, W. Schiel, E. Zarza, R. Osuna, P. Nava, EuroTrough – a new parabolic trough collector with advanced lightweight structure, in: EuroTrough Collector Qualification, ISES Solar World Congress, 2003, `https://elib.dlr.de/99768/1/EuroTrough_Ises2003_0523_final_.pdf`.

[32] V. E. Dudley, G. J. Kolb, A. R. Mahoney, T. R. Mancini, C. W. Matthews, M. Sloan, D. Kearney, Test results: SEGS LS-2 solar collector, Tech. Rep. SAND94-1884, Sandia National Laboratories, `https://www.osti.gov/servlets/purl/70756` (1994).

[33] NOAA and NASA and USAF, U.s. standard atmosphere, 1976, Tech. Rep. NOAA-S/T 76-1562, U.S. Government Printing Office (1976).